EINDHOVEN
UNIVERSITY OF
TECHNOLOGY

# Selective Area Growth of PbTe Nanowire Networks on InP

*Citation for published version (APA):*
Jung, J., Schellingerhout, S. G., Ritter, M. F., ten Kate, S. C., van der Molen, O. A. H., de Loijer, S., Verheijen, M. A., Riel, H., Nichele, F., & Bakkers, E. P. A. M. (2022). Selective Area Growth of PbTe Nanowire Networks on InP. *Advanced Functional Materials*, *32*(51), Article 2208974. https://doi.org/10.1002/adfm.202208974

*DOI:*
10.1002/adfm.202208974

*Document status and date:*
Published: 16/12/2022

*Document Version:*
Publisher’s PDF, also known as Version of Record (includes final page, issue and volume numbers)

*Please check the document version of this publication:*

• A submitted manuscript is the version of the article upon submission and before peer-review. There can be important differences between the submitted version and the official published version of record. People interested in the research are advised to contact the author for the final version of the publication, or visit the DOI to the publisher's website.
• The final author version and the galley proof are versions of the publication after peer review.
• The final published version features the final layout of the paper including the volume, issue and page numbers.

Link to publication

*General rights*
Copyright and moral rights for the publications made accessible in the public portal are retained by the authors and/or other copyright owners and it is a condition of accessing publications that users recognise and abide by the legal requirements associated with these rights.

• Users may download and print one copy of any publication from the public portal for the purpose of private study or research.
• You may not further distribute the material or use it for any profit-making activity or commercial gain
• You may freely distribute the URL identifying the publication in the public portal.

If the publication is distributed under the terms of Article 25fa of the Dutch Copyright Act, indicated by the “Taverne” license above, please follow below link for the End User Agreement:

www.tue.nl/taverne

*Take down policy*
If you believe that this document breaches copyright please contact us at:

openaccess@tue.nl

providing details and we will investigate your claim.

Download date: 16. Nov. 2023

ADVANCED FUNCTIONAL MATERIALS
www.afm-journal.de

Check for updates

# Selective Area Growth of PbTe Nanowire Networks on InP

*Jason Jung, Sander G. Schellingerhout, Markus F. Ritter, Sofieke C. ten Kate, Orson A.H. van der Molen, Sem de Loijer, Marcel A. Verheijen, Heike Riel, Fabrizio Nichele, and Erik P.A.M. Bakkers**

**Hybrid semiconductor–superconductor nanowires are promising candidates as quantum information processing devices. The need for scalability and complex designs calls for the development of selective area growth techniques. Here, the growth of large scale lead telluride (PbTe) networks is introduced by molecular beam epitaxy. The group IV-VI lead-salt semiconductor is an attractive material choice due to its large dielectric constant, strong spin-orbit coupling, and high carrier mobility. A crystal re-orientation process during the initial growth stages leads to single crystalline nanowire networks despite a large lattice mismatch, different crystal structure, and diverging thermal expansion coefficient to the indium phosphide (InP) substrate. The high quality of the resulting material is confirmed by Hall bar measurements, indicating mobilities up to 5600 cm$^2$ (Vs)$^{-1}$, and Aharonov–Bohm experiments, indicating a low-temperature phase coherence length exceeding 21 μm. Together, these properties show the high potential of the system as a basis for topological networks.**

## 1. Introduction

Research on topological quantum computation is driven by its promise of inherent fault tolerance.[1–3] One proposed material platform is hybrid semiconductor–superconductor nanowire networks,[4–7] making the growth of these networks a major goal for material scientists in the field. Preceding efforts on out-of-plane grown nanowires have resulted in ballistic transport over several microns[8,9] and indications of Majorana zero modes.[10–12] A shortcoming of this type of growth lies in its limited scalability and geometric flexibility. Selective area growth (SAG) based techniques have emerged to address these issues. Material requirements for the semiconductor include a small effective mass, a high Landé g-factor, and a large spin-orbit coupling. Consequently, most prior work has focused on InAs and InSb networks.[13–16] However, with promising results in 2D structures,[17–22] PbTe recently emerged as a potential alternative platform.[23–26] In addition to fulfilling the aforementioned requirements,[27,28] bulk PbTe has an anisotropic effective mass of $m^* = 0.024\ m_e - 0.24\ m_e$,[29] and possesses a particularly high static dielectric constant of 1350 at low temperature.[30] This suppresses long-range tails of Coulomb potentials, shielding fluctuations caused by charge impurities and dislocations.[31] These favorable properties make PbTe a strong candidate for topology based applications, where disorder is currently viewed as one of the main limitations.[32–35]

This work presents the growth of complex in-plane PbTe nanowire networks by molecular beam epitaxy (MBE). Unlike existing work,[25] growth was achieved on conventional InP substrates, overcoming the large 10.1% lattice mismatch, differing crystal structure, and diverging thermal expansion coefficient. The resulting single-crystalline networks are of high purity, have well-defined facets and junctions, and demonstrate a sharp substrate interface with no signs of reaction or atomic exchange. Transport measurements confirm the high material quality, resulting in a Hall mobility up to 5600 cm$_2$ (Vs)$^{-1}$, a g-factor of 23, and at base temperature of the setup a coherence length exceeding 21 μm, which is higher than in any previous study on SAG devices.[14–16,26,36] Overall, PbTe SAG holds high promise as a material platform for future experiments toward topological quantum computation.

## 2. Selective Area Growth

**Figure 1** introduces the SAG of PbTe. The starting point is a semi-insulating InP (111)A substrate covered by an amorphous $Si_xN_y$ mask. Lithographically defined openings are dry etched

J. Jung, S. G. Schellingerhout, O. A.H. van der Molen, S. de Loijer, M. A. Verheijen, E. P.A.M. Bakkers
Department of Applied Physics
Eindhoven University of Technology
5600 MB Eindhoven, The Netherlands
E-mail: e.p.a.m.bakkers@tue.nl

M. F. Ritter, S. C. ten Kate, H. Riel, F. Nichele
IBM Research Europe
8803 Rüschlikon, Switzerland

S. C. ten Kate
University of Twente
Drienerlolaan 5 , Enschede 7522 NB, The Netherlands

M. A. Verheijen
Eurofins Materials Science Netherlands BV
5656 AE Eindhoven, The Netherlands

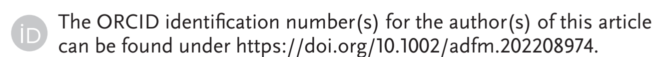
The ORCID identification number(s) for the author(s) of this article can be found under https://doi.org/10.1002/adfm.202208974.

© 2022 The Authors. Advanced Functional Materials published by Wiley-VCH GmbH. This is an open access article under the terms of the Creative Commons Attribution License, which permits use, distribution and reproduction in any medium, provided the original work is properly cited.

**DOI: 10.1002/adfm.202208974**

16163028, 2022, 51, Downloaded from https://onlinelibrary.wiley.com/doi/10.1002/adfm.202208974 by Technical University Eindhoven, Wiley Online Library on [13/06/2023]. See the Terms and Conditions (https://onlinelibrary.wiley.com/terms-and-conditions) on Wiley Online Library for rules of use; OA articles are governed by the applicable Creative Commons License

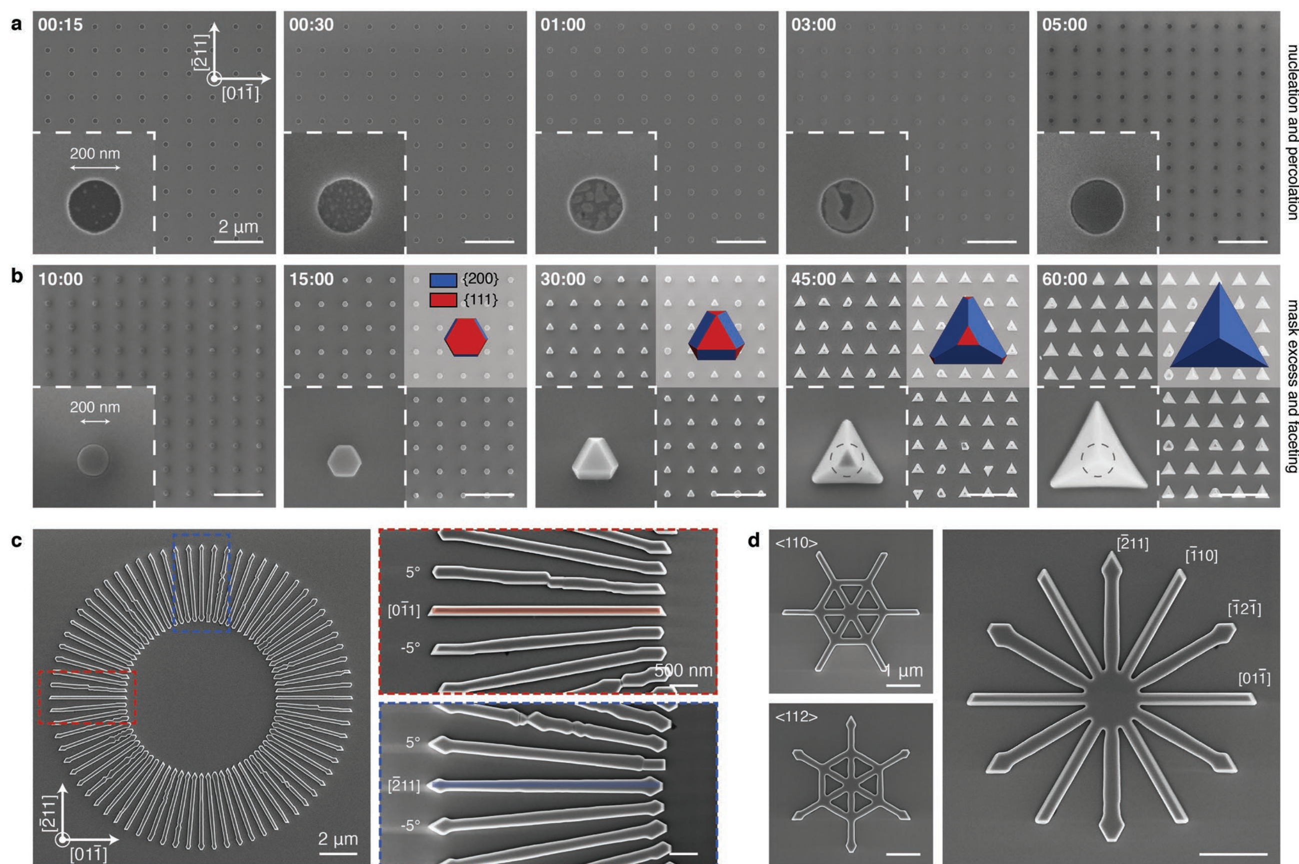


**Figure 1.** PbTe SAG on InP (111)A. a) The initial stages of growth from nucleation to island coalescence and to the formation of a closed film. Top-view SEM images show the selective area PbTe growth in a $10 \times 10$ grid of 200 nm wide circular openings for increasing growth times. Close-ups in the inset highlight the different stages of growth. The in-plane crystal directions are indicated in the first panel and kept consistent throughout, unless stated differently. b) Following film closure, the growth exceeds the mask and exhibits clear faceting. The close-ups are shown at a different scale compared to panel (a) in order to accommodate the size of the overgrowing PbTe structure. The underlying mask opening is marked by a circle for the last two time stamps. An inset in the top right of each panel shows a Wulff construction of the equilibrium crystal shape. It follows the same growth stages, illustrating the minimization of the total surface free energy and formation of low energy {200} facets. c) SEM image of 4 µm long nanowires selectively grown with their orientation rotating at an increment of 5°. All of the following examples in this figure are grown for 60 min to emphasize facet formation. Stable side facets are reliably formed in mask openings oriented along the in-plane ⟨110⟩ and ⟨112⟩ crystal directions. Close-ups of nanowire growth in these directions are shown on the right side of the panel. The colored areas indicate the underlying etched mask opening for these cases. d) Growth of nanowire networks. The top left design combines mask openings aligned along all in-plane ⟨110⟩, the bottom left all ⟨112⟩ crystal directions. The design on the right side combines the directions of both crystal families. Nanowires oriented along the ⟨112⟩ directions widen at the end to support the formation of lower energy {200} facets.

into the mask, allowing access to the underlying crystalline substrate. The correct growth conditions confine the subsequent PbTe epitaxy to these openings. Figure 1a shows scanning electron microscopy (SEM) images depicting the initial growth stages in circular mask openings of 200 nm diameter. Due to weak bonding with the substrate, the growth initially follows the Volmer–Weber model.[37] In this model, islands are formed during nucleation after reaching a critical number of adatoms. The islands subsequently expand in volume until they coalesce, percolate, and form a closed film exhibiting atomic terracing. Details on the involved mechanisms are found in the accompanying growth-focused publication.[38] Figure 1b displays the growth behavior after film closure. Upon exceeding the mask, PbTe forms distinct facets. A Wulff construction closely follows the development of the crystal shape, demonstrating the minimization of the total surface free energy via the formation of low energy {200} facets. Elongated mask openings for the growth of nanowires should therefore be aligned to the substrate crystal directions to avoid vicinal surfaces and steps,[16,39] as illustrated by Figure 1c. Uniform, well-defined facets are formed in nanowires oriented along the in-plane ⟨110⟩ or ⟨112⟩ directions. Networks can therefore be grown by combining any of these directions as depicted in Figure 1d. The correct substrate processing prior to the PbTe epitaxy is crucial. This includes the chemical and thermal removal of the native oxide, as well as a Te pre-growth treatment (see Supporting Information S1). The latter substantially improves the homogeneity of the hetero-epitaxy, likely by supporting the formation of interfacial In-Te bonds. The shape of the mask opening is not found to have an influence on the epitaxial orientation of the growth. However, decreasing the size of the opening increases the probability of forming both twin defects and alternative epitaxial


© 2022 The Authors. Advanced Functional Materials published by Wiley-VCH GmbH

16163028, 2022, 51, Downloaded from https://onlinelibrary.wiley.com/doi/10.1002/adfm.202208974 by Technical University Eindhoven, Wiley Online Library on [13/06/2023]. See the Terms and Conditions (https://onlinelibrary.wiley.com/terms-and-conditions) on Wiley Online Library for rules of use; OA articles are governed by the applicable Creative Commons License

orientations also found in nucleation islands (see Supporting Information S2).[38] PbTe SAG on InP (100) substrates exhibits similar growth dynamics, but differs in its equilibrium crystal shape and consequently in the constraints on the preferential in-plane wire orientation (see Supporting Information S3). In the previous examples, a growth time of 60 min is chosen to illustrate facet formation. This leads to overgrowth at network junctions as well as terminating {200} growth facets that widen the ends of ⟨112⟩ oriented wires. For quantum transport experiments, where one-dimensional confinement is crucial, a shorter growth time is preferred in order to keep the epitaxy strictly confined to the mask opening (see Supporting Information S4).

## 3. Material Analysis

Device performance depends on the ability to produce materials with high purity and low disorder.[40] **Figure 2** focuses on the analysis of the PbTe crystal quality. A high-resolution transmission electron microscopy (HRTEM) image of a cross section of ten parallel nanowires is introduced in Figure 2a. The growth is homogeneous, showing no sign of growth rate variation, i.e., synergetic or competitive behavior, across the examined wires.[41] A close-up of the right-most wire is depicted in Figure 2b and exposes the surface facets of the wire. An energy-dispersive X-ray (EDX) elemental mapping of the same region, shown in Figure 2c, confirms a sharp substrate-to-nanowire interface and the absence of intermixing or other local impurities down to the detection limit of the imaging technique. The InP and PbTe are imaged along the $[01\bar{1}]$ axes of their zincblende and rock-salt face-centered cubic structure. The electron diffraction pattern in Figure 2d reveals a twinned epitaxial relation between substrate and growth. Despite originating from many nucleation islands with various epitaxial orientations, the final PbTe SAG is single crystalline. This finding is supported by equivalent electron diffraction patterns taken across a 2 × 2 µm opening.[38] The underlying mechanism is a reorientation process within the initial stages of the growth, facilitating the growth of large single crystalline structures. A high-angle annular dark-field scanning TEM micrograph of the interface is shown in Figure 2e. An inverse fast Fourier transformation (iFFT) of the same region unveils the atomic columns and the misfit dislocations at the interface compensating the 10.1% lattice mismatch. Other examined nanowires show the same facets, crystal quality and epitaxial relation (see Supporting Information S5).

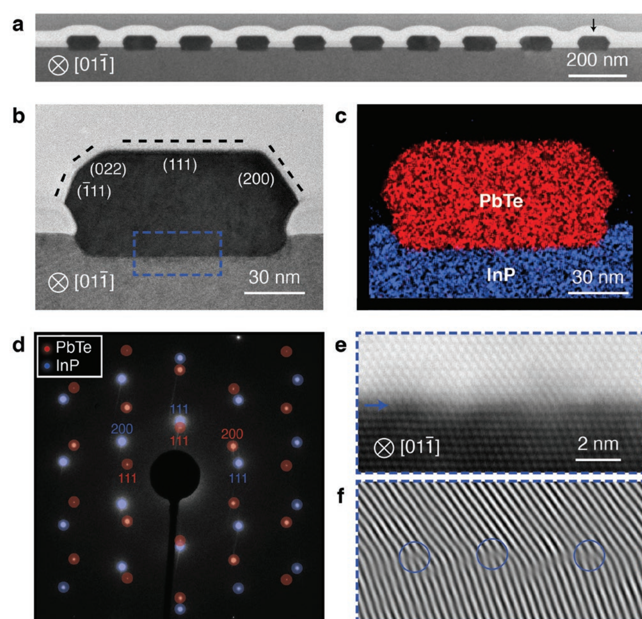


**Figure 2.** Crystal quality and interface analysis. a) Bright-field HRTEM micrograph of a cross-section cut perpendicular to the growth direction of ten parallel nanowires. b) Close-up of the right-most wire. It exhibits distinct faceting and a flat InP/PbTe interface. c) EDX elemental mapping of the same area showing no signs of intermixing between the InP substrate (blue) and the PbTe nanowire (red). d) The electron diffraction pattern of the nanowire displays the twinned epitaxial relation between InP (blue) and PbTe (red). The first order diffraction peak directions are indicated in the panel. e) High-angle annular dark-field scanning TEM micrograph of the region marked in blue in panel (b). The InP/PbTe interface is indicated with an arrow. f) An iFFT of the same region reveals the atomic columns. The 10.1% lattice mismatch between InP and PbTe is compensated by misfit dislocations directly at the interface (blue circles).

## 4. Mobility Measurements

Next, we turn to quantum transport experiments to complement the structural analysis. Two Hall bar devices were fabricated on branched nanowires of 60 nm (Hall Device 1) and 80 nm (Hall Device 2) width, respectively. **Figure 3**a shows a false-colored SEM micrograph of Hall Device 1, with Ti/Au contacts and a top gate separated by 23 nm $Al_2O_3$. Measurements were performed using low-frequency lock-in techniques at a mixing chamber temperature $T = 12$ mK. A voltage $V_{AC}$ was applied (see Experimental Section), while the longitudinal and transversal voltages $V_{xx}$ and $V_{xy}$, as well as the current $I_{AC}$ were recorded. Figure 3b displays the differential conductance $G = I_{AC}/V_{xx}$ of Hall Device 1 as a function of top gate voltage $V_{TG}$. At $B_\perp = 0$ a conductance plateau is observed with a value close to $G_0 = 2e^2h^{-1}$. At $B_\perp = 6$ T an additional step emerges at $e^2h^{-1}$ due to Zeeman splitting, visible also in the transconductance $dG/dV_{TG}$ plot of Figure 3c. A gate lever arm of 0.033 is extracted from bias spectroscopy measurements that yields a Landé g-factor of 23 from the level splitting of the first plateau, consistent with our recent study on PbTe quantum dots.[42] No conductance plateaus were observed in Hall Device 2. Assuming a rectangular nanowire cross section, we extract the longitudinal and transversal resistivities $\rho_{xx} = (V_{xx}/I_{AC}) \cdot (w_H h_H/l_H)$ and $\rho_{xy} = (V_{xy}/I_{AC}) \cdot h_H$ of Hall Device 1 as a function of $B_\perp$ at $V_{TG} = 0$. Here, $w_H$ is the width, $h_H = 50$ nm is the height, and $l_H = 1$ µm is the length of the Hall bar. The longitudinal resistivity $\rho_{xx}$ exhibits aperiodic mesoscopic fluctuations as shown in Figure 3d.[43] The transversal resistivity is $\rho_{xy} \neq 0$ at $B_\perp = 0$, similar to the average value of $\rho_{xx}$. This is attributed to the horizontal offset between opposing side arms in the device geometry, evident in Figure 3a. [44] The dependence of the Hall mobility $\mu_H$ on the electron density $n_e$ was extracted by measuring $\rho_{xx} = 1/(\mu_H e n_e)$ and $\rho_{xy} = B_\perp/(e n_e)$ as a function of $V_{TG}$, with the elementary charge $e$. The relation is shown in Figure 3e for both Hall Device 1 and Hall Device 2. The mobility reaches values of


© 2022 The Authors. Advanced Functional Materials published by Wiley-VCH GmbH

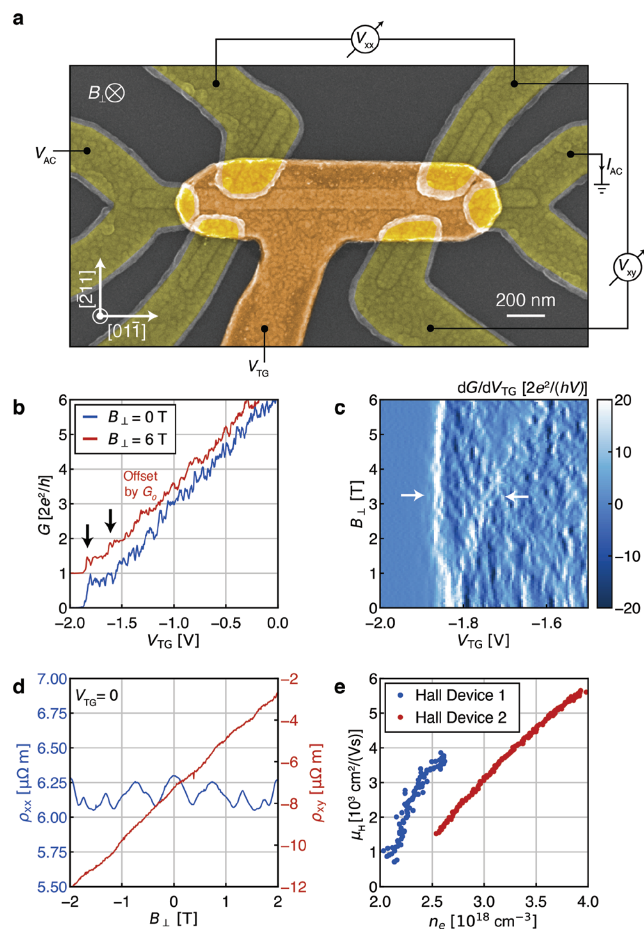


**Figure 3.** Hall measurements. a) False colored SEM micrograph of Hall Device 1 with contacts (yellow), top gate (orange), and a schematic measurement setup. b) Wire conductance $G$ as a function of the top gate voltage $V_{TG}$ at $B_\perp = 0$ and 6 T (trace offset by $G_0$). The first conductance plateau splits at high fields (black arrows). c) Transconductance $dG/dV_{TG}$ as a function of $B_\perp$ with indicated plateau splitting (white arrows). d) Longitudinal $\rho_{xx}$ and transversal resistivity $\rho_{xy}$ as a function of $B_\perp$ at $V_{TG} = 0$. e) Hall mobility $\mu_H$ versus carrier density $n_e$ of Hall Device 1 with 60 nm width and Hall Device 2 with 80 nm width.

3800 and 5600 $cm^2(Vs)^{-1}$ at $V_{TG} = 0$, corresponding to a mean free path of $l_e \approx 100$ and 180 nm, respectively. Conductance measurements on a top gated nanowire provided a field-effect mobility of $\mu_F \approx 6400$ $cm^2(Vs)^{-1}$ (see Supporting Information S6). No decrease of $\mu_H$ was observed between $T = 12$ mK and $T = 3.8$ K. This, together with a consistently higher mobility of devices with larger cross section suggests that $\mu_H$ is likely limited by interface scattering. Similar conclusions were reached in an early study of the Hall mobility in PbTe films.[45] Passivation through the addition of a CdTe shell could alleviate surface scattering, but has yielded mixed results so far.[26,46] In comparison, studies of the carrier density and mobility of PbTe films found $n_e \approx 10^{17}$ $cm^{-3}$ and $\mu_H \approx 10^6$ $cm^2$ $(Vs)^{-1}$ at 5 K.[17] In quantum wells based on doped and undoped PbTe films, mobilities of approximately $10^4 - 10^5$ $cm^2(Vs)^{-1}$ were found, higher than in our nanowire devices.[19–21] The discrepancy can likely be attributed to the reduced dimensionality of nanowire devices.

## 5. Aharonov–Bohm Experiments

Finally, we extract the electronic phase coherence length from transport measurements on a PbTe loop. A false colored SEM micrograph of the measured device is shown in **Figure 4**a. The PbTe loop has a circumference of $L = 4$ μm and a channel width of 100 nm. The resistance as a function of the perpendicular magnetic field $B_\perp$, depicted in Figure 4b, exhibits periodic oscillations. The amplitude of these oscillations decreases with increasing mixing chamber temperature $T$, as indicated in Figure 4c for the lowest and highest $T$ of an extended data set (see Supporting Information S7). The Fourier spectrum of the resistance, after subtracting a slowly varying background, is shown in Figure 4d at $T = 12$ mK. Distinct peaks are identified as $h/e$ oscillations, signature of the Aharonov–Bohm (AB) effect, $h/2e$ oscillations, signature of the Altshuler-Aronov–Spivak (AAS) effect (see Supporting Information S8), and an additional higher $h/3e$ harmonic of the AB oscillations.[47–49] Their periodicities of 5.6, 2.8, and 1.9 mT, respectively, correspond to an area of 0.74 $\mu m^2$. This is in agreement with the lithographic area 0.68 – 1.08 $\mu m^2$ of the inner and outer boundary of the loop design. The AAS effect occurs due to interference of time-reversed paths. It is consequently more robust against disorder than the AB effect and is used for an estimation of the electron phase coherence length $l_\phi(T)$.[50] Figure 4e plots the amplitude of the oscillation $A_{h/2e}$ as a function of $T$. To estimate the coherence length, $A_{h/2e}$ is fit with a model of the form[51]

$$A_{h/ne}(T) = A_0 \cdot \exp\left(-\frac{nL}{l_\phi(T)}\right) \tag{1}$$

Here, $n = 2$ is the winding number for $h/2e$ oscillations, $l_\phi(T) = C \cdot T^{-m}$ with $m = 1/2$ in the diffusive regime, and $A_0$ and $C$ are fit parameters. Extracting $A_{h/2e}$ for $|B_\perp| < 180$ mT yields a phase coherence length $l_\phi > 21$ μm at the base temperature of the setup. This long phase coherence length is consistent with reduced e-e interaction, as expected in PbTe due to its large dielectric constant.[31] Similar studies were recently conducted on SAG InAs,[14,36] InSb,[15,16] and PbTe grown on CdTe,[26] all reporting lower values for $l_\phi$.

## 6. Conclusion

Our results show the successful SAG of PbTe on InP (111)A. The developed approach is flexible in its design, scalable, and reproducible, facilitating the growth of well-defined branched nanowire networks. The structures show no signs of interface reactions and are single crystalline despite the large lattice mismatch, varying crystal structure, and diverging thermal expansion coefficient compared to the InP substrate. Transport experiments confirm the high material quality and reveal a Hall mobility up to 5600 $cm^2(Vs)^{-1}$ and a phase coherence length exceeding 21 μm at the base temperature of the setup. Together, these results indicate a promising material platform, providing a further step toward topological quantum computation.



© 2022 The Authors. Advanced Functional Materials published by Wiley-VCH GmbH

16163028, 2022, 51, Downloaded from https://onlinelibrary.wiley.com/doi/10.1002/adfm.202208974 by Technical University Eindhoven, Wiley Online Library on [13/06/2023]. See the Terms and Conditions (https://onlinelibrary.wiley.com/terms-and-conditions) on Wiley Online Library for rules of use; OA articles are governed by the applicable Creative Commons License

16163028, 2022, 51, Downloaded from https://onlinelibrary.wiley.com/doi/10.1002/adfm.202208974 by Technical University Eindhoven, Wiley Online Library on [13/06/2023]. See the Terms and Conditions (https://onlinelibrary.wiley.com/terms-and-conditions) on Wiley Online Library for rules of use; OA articles are governed by the applicable Creative Commons License

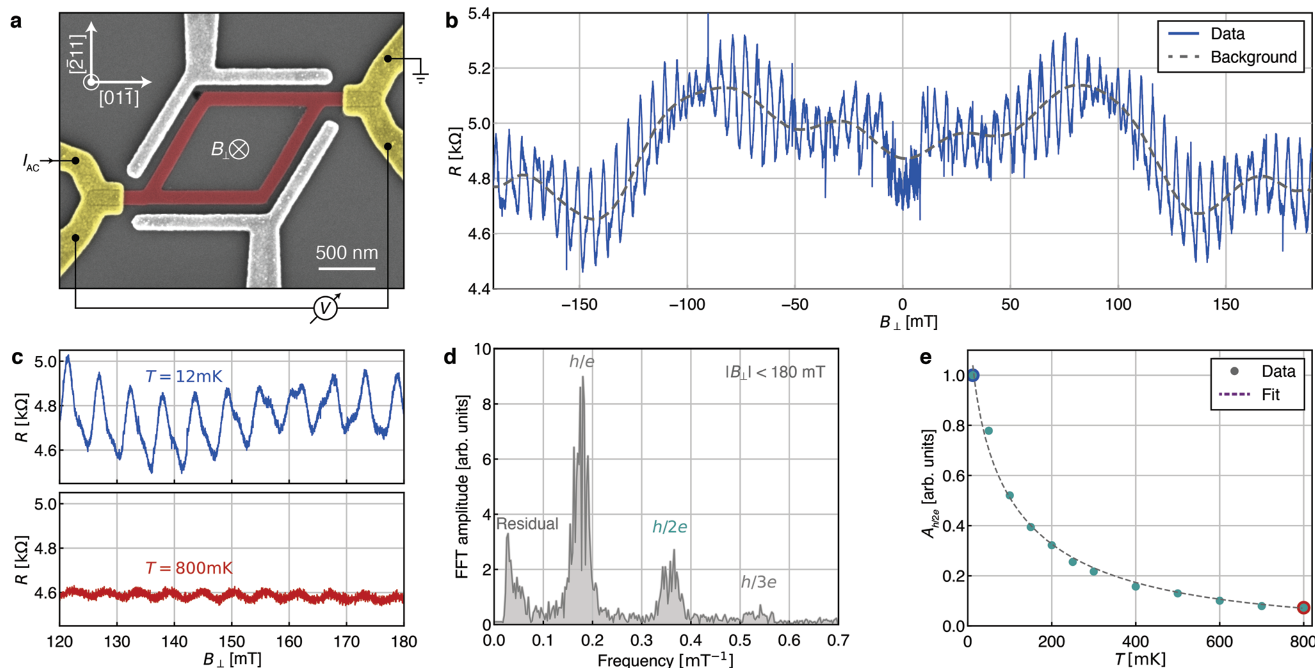


**Figure 4.** AB oscillations. a) False colored SEM micrograph of an AB device, with the PbTe network (red), contacts (yellow), and the measurement setup. The side gates (gray) were not operated in this experiment and remained grounded. b) Resistance $R$ as a function of the perpendicular magnetic field $B_\perp$. c) For increasing temperatures, the oscillations decline in amplitude. Exemplary $R$ is shown in a high field range at $T = 12$ mK (blue) and $T = 800$ mK (red). d) After subtraction of the low-frequency background (gray) depicted in (b), a Fast-Fourier spectrum of the resistance at $T = 12$ mK reveals distinct $h/e$, $h/2e$ and $h/3e$ peaks. The corresponding amplitudes can be extracted by applying a Gaussian window centered around the period and integrating the signal. The additional peak in the Fourier spectrum at low-frequency is attributed to residual magnetoconductance components after the background subtraction. e) The amplitude of the $h/2e$ oscillations as a function of $T$ with an exponential fit (purple) that enables the estimation of the phase coherence length.

## 7. Experimental Section

*Substrate Fabrication*: Electron-beam lithography (EBL) markers were etched into undoped semi-insulating (111)A and (100) InP substrates by reactive-ion etching using $CHF_3$ with added $O_2$.[39] Subsequently, 20 nm $Si_xN_y$ was deposited by plasma-enhanced chemical vapor deposition (PECVD). AR-P 6200.13 resist was spun at 4000 rpm on the chip, and baked at 150 °C for 60 s. The mask openings were written by EBL and developed in AR 600-546 for 60 s. Reactive ion etching transferred the pattern into the mask. A phosphoric acid wet etch ($H_2O : H_3PO_4 = 10 : 1$) removed the native substrate oxides, after which the substrates were loaded into the MBE and degassed at 300 °C for 1 h.

*PbTe Heteroepitaxy*: Growth took place in an ultra-high vacuum MBE system. An annealing step under Te overpressure at 480 °C was used for surface reconstruction of the etched openings and to remove oxide residuals from the exposed substrate surface. The PbTe networks were subsequently grown at 340 °C with separate elemental sources, providing a Te flux of $4.00 \times 10^{-7}$ mbar and a Pb flux of $1.25 \times 10^{-7}$ mbar measured as beam equivalent pressure using a naked bayard-alpert ion gauge. Temperatures were measured with a kSA BandiT system based on the optical absorption edge.

*Wulff Construction*: The visualization of crystal equilibrium shapes was based on WulffMaker.[52] The ratio of the surface energies $\gamma_{\{200\}}/\gamma_{\{111\}}$ was chosen for each growth time stamp to best represent the experimentally found shape.

*TEM Studies*: TEM studies were performed using a probe-corrected JEOL ARM 200F, equipped with a 100 $mm^2$ Centurio SDD Energy dispersive X-ray spectroscopy detector. Misfit dislocations at the InP-PbTe interface were visualized by first creating an FFT of an atomic resolution image, then applying a filter to only include one InP (111) and the adjacent PbTe (200) spot, and finally creating an iFFT of the result.

*Device Fabrication*: A PMMA double layer resist of 200 nm AR-P 669.04 and 50 nm AR-P 672.02 was spun on the chip, and each layer was baked at 180 °C for 5 min. Contacts were exposed using EBL, followed by development in MIBK:IPA (1:2) and rinsing in IPA. Native oxides of PbTe were etched by ex situ Ar sputtering. Subsequently 5 nm Ti and 50 nm Au were evaporated. Lift-off was performed in acetone. On devices with top gates, a 23 nm layer of $Al_2O_3$ was deposited using thermal atomic layer deposition at 110 °C, followed by EBL, evaporation and lift-off with the same parameters as for contacts.

*Electrical Measurements*: Measurements were performed with standard low-frequency lock-in techniques in a dilution refrigerator with a mixing chamber temperature of $T = 12$ mK. For measurements in Figure 3b,c,e, an AC voltage between 3 and 10 µV was applied, and the device was grounded via a low-impedance IV converter, which measured the current. Measurements in Figure 3d were recorded by sourcing a current of 10 nA and recording the transversal and longitudinal voltages. The mean free path $l_e = (\mu_H m^* v_F)/e$ was calculated using the Fermi velocity $v_F = (\hbar k_F)/m^*$ and the Fermi wave vector $k_F = (3\pi^2 n_e)^{1/3}$. In Figure 4, an AC current with amplitude 400 pA was passed in the device, and the resulting voltage drop was amplified and measured. In Figure 4c, single outliers were removed from the raw data presented in Figure 4b. An outlier was defined as a data point with a value three standard deviations away from the median of a moving window containing ten data points. Each plotted data point was the average of four measurements in the raw data. The amplitude $A_{h/2e}$ was extracted by applying a Gaussian window to the Fourier spectrum centered around the $h/2e$ period and integrating the signal.

## Supporting Information

Supporting Information is available from the Wiley Online Library or from the author.


© 2022 The Authors. Advanced Functional Materials published by Wiley-VCH GmbH

16163028, 2022, 51, Downloaded from https://onlinelibrary.wiley.com/doi/10.1002/adfm.202208974 by Technical University Eindhoven, Wiley Online Library on [13/06/2023]. See the Terms and Conditions (https://onlinelibrary.wiley.com/terms-and-conditions) on Wiley Online Library for rules of use; OA articles are governed by the applicable Creative Commons License


## Acknowledgements

J.J. and S.G.S. contributed equally to this work. The authors thank A. Fuhrer and W. Riess for the fruitful discussions. Additional thanks goes to NanoLab@TU/e and the cleanroom operations team of the Binnig and Rohrer Nanotechnology Center (BRNC) for their help and support. This work was supported by the European Research Council (ERC TOCINA 834290). F.N. acknowledges the European Research Council (Grant No. 804273) and the Swiss National Science Foundation (Grant No. 200021_201082). The authors recognize Solliance, a solar energy R&D initiative of ECN, TNO, Holst, TU/e, IMEC and Forschungszentrum Jülich, and the Dutch province of Noord-Brabant for funding the TEM facility.


## Conflict of Interest

The authors declare no conflict of interest.

## Data Availability Statement

The data that support the findings of this study are openly available in Zenodo at https://doi.org/10.5281/zenodo.6900881, reference number 6900881.


## Keywords

nanowires, PbTe, topological quantum computations

Received: August 4, 2022
Revised: September 2, 2022
Published online: October 17, 2022



[1] A. Kitaev, *Ann. Phys.* **2003**, *303*, 2.
[2] C. Nayak, S. H. Simon, A. Stern, M. Freedman, S. D. Sarma, *Rev. Mod. Phys.* **2008**, *80*, 1083.
[3] S. D. Sarma, M. Freedman, C. Nayak, *npj Quantum Information* **2015**, *1*, 15001.
[4] R. M. Lutchyn, J. D. Sau, S. D. Sarma, *Phys. Rev. Lett.* **2010**, *105*, 077001.
[5] Y. Oreg, G. Refael, F. v. Oppen, *Phys. Rev. Lett.* **2010**, *105*, 177002.
[6] T. Karzig, C. Knapp, R. M. Lutchyn, P. Bonderson, M. B. Hastings, C. Nayak, J. Alicea, K. Flensberg, S. Plugge, Y. Oreg, C. M. Marcus, M. H. Freedman, *Phys. Rev. B* **2017**, *95*, 235305.
[7] S. Plugge, A. Rasmussen, R. Egger, K. Flensberg, *New J. Phys.* **2017**, *19*, 012001.
[8] I. v. Weperen, S. R. Plissard, E. P. A. M. Bakkers, S. M. Frolov, L. P. Kouwenhoven, *Nano Lett.* **2013**, *13*, 387.
[9] J. Kammhuber, M. C. Cassidy, H. Zhang, O. Gül, F. Pei, M. W. A. d. Moor, B. Nijholt, K. Watanabe, T. Taniguchi, D. Car, S. R. Plissard, E. P. A. M. Bakkers, L. P. Kouwenhoven, *Nano Lett.* **2016**, *16*, 3482.
[10] V. Mourik, K. Zuo, S. M. Frolov, S. R. Plissard, E. P. A. M. Bakkers, L. P. Kouwenhoven, *Science* **2012**, *336*, 1003.
[11] S. M. Albrecht, A. P. Higginbotham, M. Madsen, F. Kuemmeth, T. S. Jespersen, J. Nygård, P. Krogstrup, C. M. Marcus, *Nature* **2016**, *531*, 206.
[12] M. T. Deng, S. Vaitiekėnas, E. B. Hansen, J. Danon, M. Leijnse, K. Flensberg, J. Nygård, P. Krogstrup, C. M. Marcus, *Science* **2016**, *354*, 1557.
[13] F. Krizek, J. E. Sestoft, P. Aseev, S. Marti-Sanchez, S. Vaitiekėnas, L. Casparis, S. A. Khan, Y. Liu, T. Stankevič, A. M. Whiticar, A. Fursina, F. Boekhout, R. Koops, E. Uccelli, L. P. Kouwenhoven, C. M. Marcus, J. Arbiol, P. Krogstrup, *Phys. Rev. Mater.* **2018**, *2*, 093401.
[14] J. S. Lee, S. Choi, M. Pendharkar, D. J. Pennachio, B. Markman, M. Seas, S. Koelling, M. A. Verheijen, L. Casparis, K. D. Petersson, I. Petkovic, V. Schaller, M. J. W. Rodwell, C. M. Marcus, P. Krogstrup, L. P. Kouwenhoven, E. P. A. M. Bakkers, C. J. Palmstrøm, *Phys. Rev. Mater.* **2019**, *3*, 084606.
[15] P. Aseev, G. Wang, L. Binci, A. Singh, S. Martí-Sánchez, M. Botifoll, L. J. Stek, A. Bordin, J. D. Watson, F. Boekhout, D. Abel, J. Gamble, K. V. Hoogdalem, J. Arbiol, L. P. Kouwenhoven, G. d. Lange, P. Caroff, *Nano Lett.* **2019**, *19*, 9102.
[16] R. L. M. O. h. Veld, D. Xu, V. Schaller, M. A. Verheijen, S. M. E. Peters, J. Jung, C. Tong, Q. Wang, M. W. A. d. Moor, B. Hesselmann, K. Vermeulen, J. D. S. Bommer, J. S. Lee, A. Sarikov, M. Pendharkar, A. Marzegalli, S. Koelling, L. P. Kouwenhoven, L. Miglio, C. J. Palmstrøm, H. Zhang, E. P. A. M. Bakkers, *Commun. Phys.* **2020**, *3*, 59.
[17] G. Springholz, G. Bauer, G. Ihninger, *J. Cryst. Growth* **1993**, *127*, 302.
[18] G. Grabecki, J. Wróbel, T. Dietl, K. Byczuk, E. Papis, E. Kamińska, A. Piotrowska, G. Springholz, M. Pinczolits, G. Bauer, *Phys. Rev. B* **1999**, *60*, R5133.
[19] G. Grabecki, J. Wróbel, T. Dietl, E. Papis, E. Kamińska, A. Piotrowska, A. Ratuszna, G. Springholz, G. Bauer, *Phys. E* **2004**, *20*, 236.
[20] V. A. Chitta, W. Desrat, D. K. Maude, B. A. Piot, N. F. Oliveira, P. H. O. Rappl, A. Y. Ueta, E. Abramof, *Phys. Rev. B* **2005**, *72*, 195326.
[21] V. Chitta, W. Desrat, D. Maude, B. Piot, N. Oliveira, P. Rappl, A. Ueta, E. Abramof, *Phys. E* **2006**, *34*, 124.
[22] G. Grabecki, J. Wróbel, T. Dietl, E. Janik, M. Aleszkiewicz, E. Papis, E. Kamińska, A. Piotrowska, G. Springholz, G. Bauer, *Phys. E* **2006**, *34*, 560.
[23] S. G. Schellingerhout, E. J. d. Jong, M. Gomanko, X. Guan, Y. Jiang, M. S. M. Hoskam, J. Jung, S. Koelling, O. Moutanabbir, M. A. Verheijen, S. M. Frolov, E. P. A. M. Bakkers, *Materials for Quantum Technology* **2022**, *2*, 015001.
[24] Z. Cao, D. E. Liu, W.-X. He, X. Liu, K. He, H. Zhang, *Phys. Rev. B* **2022**, *105*, 085424.
[25] Y. Jiang, S. Yang, L. Li, W. Song, W. Miao, B. Tong, Z. Geng, Y. Gao, R. Li, F. Chen, Q. Zhang, F. Meng, L. Gu, K. Zhu, Y. Zang, R. Shang, Z. Cao, X. Feng, Q.-K. Xue, D. E. Liu, H. Zhang, K. He, *Phys. Rev. Mater.* **2022**, *6*, 034205.
[26] Z. Geng, Z. Zhang, F. Chen, S. Yang, Y. Jiang, Y. Gao, B. Tong, W. Song, W. Miao, R. Li, Y. Wang, Q. Zhang, F. Meng, L. Gu, K. Zhu, Y. Zang, L. Li, R. Shang, X. Feng, Q.-K. Xue, K. He, H. Zhang, *arXiv* **2021**.
[27] C. K. N. Patel, R. E. Slusher, *Phys. Rev.* **1968**, *177*, 1200.
[28] M. L. Peres, V. A. Chitta, D. K. Maude, N. F. Oliveira, P. H. O. Rappl, A. Y. Ueta, E. Abramof, *Acta Phys. Pol. A* **2011**, *119*, 602.
[29] E. Ridolfi, E. A. d. A. e. Silva, G. C. L. Rocca, *Phys. Rev. B* **2015**, *91*, 085313.
[30] S. Yuan, H. Krenn, G. Springholz, Y. Ueta, G. Bauer, P. J. McCann, *Phys. Rev. B* **1997**, *55*, 4607.
[31] G. Grabecki, J. Wróbel, T. Dietl, E. Janik, M. Aleszkiewicz, E. Papis, E. Kamińska, A. Piotrowska, G. Springholz, G. Bauer, *Phys. Rev. B* **2005**, *72*, 125332.
[32] H. Pan, S. D. Sarma, *Phys. Rev. Res.* **2020**, *2*, 013377.
[33] S. D. Sarma, H. Pan, *Phys. Rev. B* **2021**, *103*, 195158.
[34] S. Ahn, H. Pan, B. Woods, T. D. Stanescu, S. D. Sarma, *Phys. Rev. Mater.* **2021**, *5*, 124602.
[35] B. D. Woods, S. D. Sarma, T. D. Stanescu, *Phys. Rev. Appl.* **2021**, *16*, 054053.



© 2022 The Authors. Advanced Functional Materials published by Wiley-VCH GmbH

[36] S. Vaitiekėnas, A. M. Whiticar, M.-T. Deng, F. Krizek, J. E. Sestoft, C. J. Palmstrøm, S. Marti-Sanchez, J. Arbiol, P. Krogstrup, L. Casparis, C. M. Marcus, *Phys. Rev. Lett.* **2018**, *121*, 147701.
[37] M. Volmer, A. Weber, *Zeitschrift für Physikalische Chemie* **1926**, *119U*, 277.
[38] J. Jung, S. Schellingerhout, O. van der Molen, W. Peeters, M. Verheijen, E. Bakkers, *arXiv* **2022**.
[39] H. Jung, D.-Y. Park, F. Xiao, K. H. Lee, Y.-H. Choa, B. Yoo, N. V. Myung, *J. Phys. Chem. C* **2011**, *115*, 2993.
[40] A. Prinz, G. Brunthaler, Y. Ueta, G. Springholz, G. Bauer, G. Grabecki, T. Dietl, *Phys. Rev. B* **1999**, *59*, 12983.
[41] M. E. Cachaza, A. W. Christensen, D. Beznasyuk, T. Særkjær, M. H. Madsen, R. Tanta, G. Nagda, S. Schuwalow, P. Krogstrup, *Phys. Rev. Mater.* **2021**, *5*, 094601.
[42] S. C. Kate, M. F. Ritter, A. Fuhrer, J. Jung, S. G. Schellingerhout, E. P. A. M. Bakkers, H. Riel, F. Nichele, *Nano Lett.* **2022**, *22*, 7049.
[43] C. Beenakker, H. v. Houten, *Solid State Phys.* **1991**, *44*, 1.
[44] J. P. DeGrave, D. Liang, S. Jin, *Nano Lett.* **2013**, *13*, 2704.
[45] J. N. Zemel, J. D. Jensen, R. B. Schoolar, *Phys. Rev.* **1965**, *140*, A330.
[46] G. Badawy, B. Zhang, T. Rauch, J. Momand, S. Koelling, J. Jung, S. Gazibegovic, O. Moutanabbir, B. J. Kooi, S. Botti, M. A. Verheijen, S. M. Frolov, E. P. A. M. Bakkers, *Adv. Sci.* **2022**.
[47] Y. Aharonov, D. Bohm, *Phys. Rev.* **1959**, *115*, 485.
[48] R. A. Webb, S. Washburn, C. P. Umbach, R. B. Laibowitz, *Phys. Rev. Lett.* **1985**, *54*, 2696.
[49] B. Al'tshuler, A. Aronov, B. Spivak, *Jetp. Lett.* **1981**, *33*, 94.
[50] S. Washburn, R. A. Webb, *Adv. Phys.* **1986**, *35*, 375.
[51] F. Milliken, S. Washburn, C. Umbach, R. Laibowitz, R. Webb, *Phys. Rev. B* **1987**, *36*, 4465.
[52] R. V. Zucker, D. Chatain, U. Dahmen, S. Hagége, W. C. Carter, *J. Mater. Sci.* **2012**, *47*, 8290.


© 2022 The Authors. Advanced Functional Materials published by Wiley-VCH GmbH

16163028, 2022, 51, Downloaded from https://onlinelibrary.wiley.com/doi/10.1002/adfm.202208974 by Technical University Eindhoven, Wiley Online Library on [13/06/2023]. See the Terms and Conditions (https://onlinelibrary.wiley.com/terms-and-conditions) on Wiley Online Library for rules of use; OA articles are governed by the applicable Creative Commons License